Energy Reports 10 (2023) 99–113

Contents lists available at ScienceDirect

Energy Reports

journal homepage: www.elsevier.com/locate/egyr

Research paper

# Chemical and thermal performance analysis of a solar thermochemical reactor for hydrogen production via two-step WS cycle

Jeet Prakash Sharma [a], Ravinder Kumar [a,*], Mohammad H. Ahmadi [b,*], Azfarizal Mukhtar [c], Ahmad Shah Hizam Md Yasir [d], Mohsen Sharifpur [e,f,**], Bulbul Ongar [g], Anara Yegzekova [h]

[a] School of Mechanical Engineering, Lovely Professional University, Phagwara-144411, Punjab, India
[b] Faculty of Mechanical Engineering, Shahrood University of Technology, Shahrood, Iran
[c] Institute of Sustainable Energy, Putrajaya Campus, Universiti Tenaga Nasional, Jalan IKRAM-UNITEN, 43000 Kajang, Malaysia
[d] Rabdan Academy, 65, Al Inshirah, Al Sa'adah, Abu Dhabi, 22401, PO Box: 114646, Abu Dhabi, United Arab Emirates
[e] Department of Mechanical and Aeronautical Engineering, University of Pretoria, Pretoria, 0002, South Africa
[f] Department of Medical Research, China Medical University Hospital, China Medical University, Taichung, Taiwan
[g] Department of Power Engineering, Satbayev University, 22a Satpaev str., Almaty, 050013, Kazakhstan
[h] Department of Power Engineering, Logistics and Transport Academy, 97 Shevchenko str, Almaty, 050012, Kazakhstan

ARTICLE INFO

*Article history:*
Received 30 March 2023
Received in revised form 5 June 2023
Accepted 8 June 2023
Available online 27 June 2023

*Keywords:*
STCR modelling
Porous media
Thermal analysis
Solar fuels
WS process
SolTrace

ABSTRACT

Ceria-based $H_2O/CO_2$-splitting solar-driven thermochemical cycle produces hydrogen or syngas. Thermal optimization of solar thermochemical reactor (STCR) improves the solar-to-fuel conversion efficiency. This research presents two conceptual designs and thermal modelling of RPC-ceria-based STCR cavities to attain the optimal operating conditions for $CeO_2$ reduction step. Presented hybrid geometries consisting of cylindrical–hemispherical and conical frustum–hemispherical structures. The focal point was positioned at x = 0, -10 mm, and -20 mm from the aperture to examine the flux distribution in both solar reactor configurations. Case-1 with 2 milliradian S.E (slope error) yields a 27% greater solar flux than case-1 with 4 milliradians S.E, despite the 4 milliradian S.E produces an elevated temperature in the reactor cavity. The mean temperature in the reactive porous region was most significant for case-2 (x = -10 mm) with 4 mrad S.E for model-2, reaching 1966 K and 2008 K radially and axially, respectively. In case-2 (x = -10 mm) for 4 mrad S.E, model-1 attained 1720 K. The efficiency analysis shows that the highest conversion efficiency value was obtained to be 7.95% for case-1 with 4 milliradian S.E.



## 1. Introduction

Solar power is a prominent and sustainable energy resource to be used in household and industrial applications (Sandoval et al., 2019). Solar technology is used to produce electricity using PV cells and generate heat using solar thermal collectors (Widyolar, 2019). Concentrating solar systems use solar energy to generate heat at different temperature levels i.e. low, medium, or high (Lilliestam et al., 2017). The application of solar technologies is different according to their operating temperature range. The parabolic trough and Linear Fresnel Reflector (LFR) are linear solar concentrators having an operational temperature of 500 °C. While the solar tower and dish systems can operate at very amplified temperatures (Fuqiang et al., 2017; Jafrancesco, 2018). This wide range of applications of solar tower in power generation and solar dishes in high temperature-based applications makes it the most promising renewable energy technology (Hafez et al., 2017). Solar dish systems are used to generate power used in cooling, heating, and chemical processes (Gavagnin et al., 2017; Moradi and Mehrpooya, 2017; Mehrpooya et al., 2018; jia et al., 2018; Dähler, 2018). The study by Khan et al. (2019) exhibited that the $Al_2O_3$/Oil-based nanofluid yields a maximum efficiency of 33.72%. Solar concentrator coupled with the stirling engine reported the system efficiency to be 10.4% and 19% (Barreto and Canhoto, 2017). The solar dish systems are designed to produce heat to be used in high-temperature-based applications.

The solar concentrating technologies such as LFR, CPC, PTC and solar dish with and without the application of nanofluids were studied by Bellos and Tzivanidis (2019). Solar collector using nanofluids by Rasih et al. (2019) proposed that the application of nanofluids is able to enhance the thermal efficiency of CPC and LFR. An investigation on the effects of Cu−$H_2O$ nanofluid on PTC

* Corresponding authors.
** Corresponding author at: Department of Mechanical and Aeronautical Engineering, University of Pretoria, Pretoria, 0002, South Africa.
*E-mail addresses:* rav.chauhan@yahoo.co.in (R. Kumar), mohammadhosein.ahmadi@gmail.com (M.H. Ahmadi), mohsen.sharifpur@up.ac.za (M. Sharifpur).

https://doi.org/10.1016/j.egyr.2023.06.012

showed that the Nusselt number (*Nu*) relies on Cu nanoparticle concentration, and decreasing Reynolds number enhances heat transfer as Cu concentration declines (Hong et al., 2020). The maximum thermal efficiency of an LFR with an evacuated tube receiver was increased by 1%. Fins also improve thermal efficiency better than nanofluids (Bellos et al., 2019). The thermal efficiency of PTC was enhanced using the conical strips and the results predicted that the value of Nu advanced up to 91.95% and its thermal performance was at best at $Re = 8000$. Solar energy is available in abundance, inexhaustible, and has usage flexibility in household and in industries. Solar thermochemical cycles convert solar energy into solar fuels (hydrogen or syngas) by splitting $H_2O$ or $CO_2$.

High-performance cork-templated ceria produced $H_2$ via a two-step $H_2O$ splitting cycle. The study pointed out that the major challenge is to develop such materials that can withstand extremely high temperatures and h redox chemical kinetics and activity at relatively low temperatures. The study also revealed cork-templated $CeO_2$ enhances the performance extensively. The increasing reduction temperature by 50 °C results in the peak $H_2$ generation rate (Costa Oliveira et al., 2020). Jia Zeng et al. studied the direct solar thermochemical conversion of methanol to hydrogen at low temperatures (Zeng et al., 2020). The study reveals that nanoscopic catalysts improve direct solar thermochemical conversion ($CuO/ZnO/Al_2O_3$). Ezbiri et al. evaluated $Y_{0.5}Ba_{0.5}CoO_3$'s oxygen production and separation redox performance (Ezbiri et al., 2020). It was pointed out that $Y_{0.5}Ba_{0.5}CoO_{3-\delta}$ has better performance than CuO. This compound has the greatest reaction rate, maximum $O_2$ exchange capacity, and minimum reaction temperature. Tou et al. demonstrated the first solar-based $CO_2$ and $H_2O$ co-thermolysis (Tou et al., 2019). Gaseous $H_2O/CO_2$ mixtures were passed across a non-stoichiometric ceria ($CeO_{2-\delta}$) membrane with 4200 suns of solar focused radiation. Isothermal (1723–1873 K) and isobaric (0.2–1.7 Pa $O_2$) conditions were used to enhance the hydrogen generation rate. Dou (2019) studied the issues and challenges in hydrogen production via thermochemical biomass conversion. The study pointed out that Ni-based catalysts are important for economically viable hydrogen production.

Ardo (2018) presented a broad view on implementing solar-based hydrogen production technologies. It was pointed out that in the long run solar hydrogen technologies will have to compete against the fossil fuel market in various aspects and the main challenge will be to keep the fuel cost to a minimum. Marxer et al. (2017) experimentally investigated the solar thermochemical-based $CO_2$ splitting into different streams of CO and $O_2$. This study was conducted using the solar reactor (4-kW) consisting of an RPC catalyst structure under the exposer of 3000x flux irradiation. The result of the study proposed the highest ever measured conversion efficiency of 5.3%. Qibin Zhu and Yimin Xuan simulated heat and fluid transport in volumetric solar reactors (Zhu and Xuan, 2017). Results demonstrated the small incidence angle enhances radiation propagation, and pore diameter affects the pressure drop. Shaner et al. (2016) compared solar-based hydrogen's techno-economics and revealed that low-$CO_2$ fossil fuel is cheaper than solar or wind. Directly converting $CO_2$ into hydrocarbon gasoline will require novel transportation and storage ideas. Herron et al. (2015) presented the general framework to assess solar fuel technologies. They discussed the catalytic conversion and direct reduction of $CO_2$. Bork et al. (2015) showed the perovskite splits $CO_2$ 25 times more than ceria. Scheffe et al. (2013) studied cobalt ferrite–zirconia oxidation and analzyed the II-order reaction and diffusion processes transpire concurrently but at distinct oxidation rate. Furler et al. (2012) investigated the $H_2O$ and $CO_2$ splitting for syngas production using ceria. They directly exposed ceria felt to the concentrated radiation of 2865 suns. Result show the fuel production 5.88 ± 0.43 mL/g $CeO_2$ in ten consecutive cycles. Roeb et al. (2011) presented an overview in solar fuel technologies and trends. It was pointed out that the application of CSP technology as primary energy source can help in reducing the carbon foot print while increasing the electricity generation.

Researchers have extensively explored the geometrical influence on the thermal performance of the reactor cavity. Jilte et al. showed the conical cavity reported the lowest convective losses compared to other shapes (Jilte et al., 2017). A study on the volumetric receiver showed the loss of 12% of the input energy through thermal losses (Harris and Lenz, 1985). Li et al. investigated the parabolic dish systems and the results showed that the optical efficiency depends upon cavity aperture radius and focal distance (Li et al., 2013). A study on 3 cavity geometrical configurations with MCRT exhibited that the solar flux varies with the geometrical aspect. It has been proved that cavity orientation has a significant effect on convective losses, radiative losses, and optical losses (Daabo et al., 2016, 2019, 2017; Pavlovic et al., 2017; Cui et al., 2013).

Dish system performance is affected by the exterior and geometrical parameters of the cavity, such as the aspect ratio and wall absorptivity (Li et al., 2016). Kulahli et al. (2019) investigated a novel reflective paraboloid design with adjustable focal distance and reported that thermal behaviour is affected by the non-uniform axial distribution of solar irradiation around the absorber. Results also reported that the flow rate optimization increases thermal efficiency by 0.21% and net energy gain by 0.63% based on parametric studies. $CO_2$ photoreduction in a twin reactor was modelled using a 2D axisymmetric multiphysics model and it was seen that the bubble flow pattern, gas–liquid interface, and catalyst surface area affect $CH_3OH$ yield (Lu et al., 2021). SPTR performance with steady and varying solar flux is also explored. The redesigned tube and short intake cone-frustum tube function better than the original tube, resulting in a 67% decrease in catalyst use. The redesigned tube enhances $CH_3OH$ conversion efficiency of 4.3%, solar-to-fuel efficiency 8.2%, and $H_2$ generation 2.4% in comparison to the conventional tube (Tang et al., 2022).

An EPCM-filled solar reactor under constant solar radiation can maintain elevated $CH_3OH$ conversion efficiency (0.93%) (Ma et al., 2021). Two case studies compare the new SRs to the current ones. The homogeneity of solar flux dispersion may be enhanced by up to 90% for the current SR design, far greater than previous systems (Tang et al., 2021). A novel receiver–reactor idea blends proven systems with high-efficiency principles. By eliminating cyclical heating of the solar reactor, the system forecasts an efficiency of over 14% for non-optimized designs. Simple implementations of the heat recovery system model up to 20% heat recovery (Brendelberger et al., 2022). Barreto et al. (2018) examined the volumetric porous structure-based receiver and the results showed the effects of the optical thickness of porous media and inclination angle. The aspect ratio, incident radiation, and system error also affect the flux on the cavity receiver walls (Mao et al., 2014). The study performed by Huang et al. (2013) confirmed that a concentration ratio above 3000 can be achieved if the S.E. was kept less than 4 mrad. Garrido et al. (2018) reported a dish-Stirling system's analyses for four receiver cavities shapes using the MCRT method.

According to the preceding research, the influence of focal distance on the solar flux and temperature profile in STCR cavities is not significantly available. The present study aims the following objectives:

1. The optical analysis of STCR to explore the effect of varying focal distance on thermal performance using the MCRT method.
2. To analyse the geometrical parameter influence on the thermal performance of the STCR cavity.

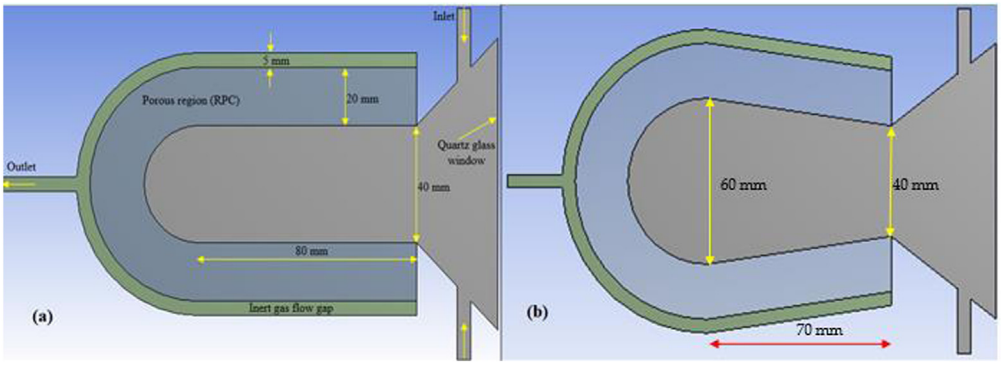


**Fig. 1.** STCR design; (a) STCR-1 and (b) STCR-2.

3. To characterize the impact of S.E on thermal parameters integrated with reactor cavity shape and focal point shift using CFD-SolTrace technique.

A time-independent analysis was carried out on two hybrids, cylindrical–hemispherical and conical frustum–hemispherical, cavity shapes model to explore the effects of cavity shape on the thermal parameters in STCR cavity. The analysis of focal distance is a crucial factor to determine the temperature profile inside the solar thermochemical reactor and to evaluate the required temperature to start the redox reactions. Thus, the results of the presented study will be helpful to design an efficient model of solar thermochemical reactors.

## 2. Methodology and STCR model description

Non-stoichiometric ceria ($CeO_{2-X}$) thermochemical cycles have been studied extensively (Montini et al., 2016; Otake et al., 2003). Numerous investigations have examined ceria's capabilities for reduction and fuel generation. To minimize the needed operating temperature, researchers have concentrated on minimizing the operating temperature difference between the steps of ceria-based redox cycles. The reactions for ceria based thermochemical cycle have been given below;

***Ceria reduction reaction***

$$CeO_2 \rightarrow CeO_{2-\delta} + \frac{\delta}{2}O_2 \quad (1)$$

***Water splitting reaction***

$$CeO_{2-\delta} + \delta H_2O \rightarrow CeO_2 + \delta H_2 \quad (2)$$

***Carbon dioxide splitting reaction***

$$CeO_{2-\delta} + \delta CO_2 \rightarrow CeO_2 + \delta CO \quad (3)$$

In the presented study, two models of the solar thermochemical reactor (Fig. 1) cavities were proposed to investigate the influences of geometrical factors on its thermal performance. Solar irradiation enters the STCR and heats the porous region to induce the reduction reaction. The argon (Ar) gas is fed into the reactor cavity through the inlets to sweep the remains of hydrogen or oxygen from the cavity. The RPC thickness was kept at 20 mm with a 5 mm wide inert gas flow divot. This investigation is structured in three cases based on focal point variation ($X = 0, -10$ mm, $-20$ mm) from the aperture as shown in Fig. 2.

A quartz window is positioned in front of the cavity opening to facilitate solar irradiation to enter the reactor. The solar flux on the quartz glass window is applied using a user-defined function: UDF solar flux profile. Inlets and outlets are provided in the cavity for the circulation of flowing fluids. As the solar flux radiates the

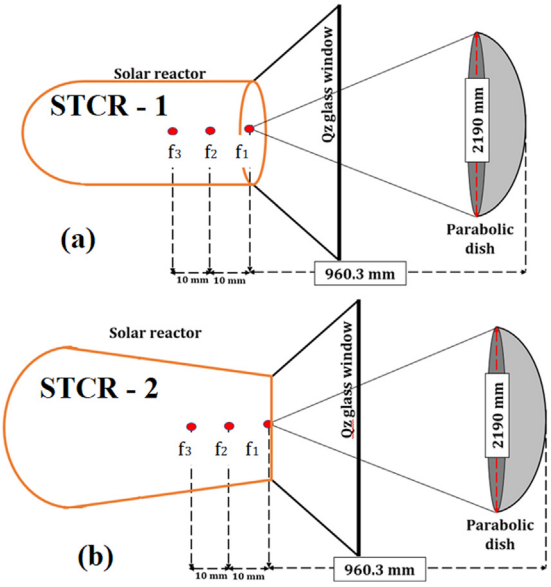


**Fig. 2.** Schematic of two STCR cavity shapes and three cases considered for each model.

cavity and increases its temperature, the flowing fluid is injected from the inlet, passes through the porous media and exits from the outlet. The flowing fluid allows the temperature profile to be distributed uniformly in the porous region. The outer region of the cavity is packed in a stainless-steel shell, and outer layers are made fully insulated to reduce the thermal loss. As some geometric factors influence the thermal efficiency of the solar thermochemical cavity. This study is focused on the investigation of geometrical factors and their influence on the thermal and optical performance of proposed solar reactor designs.

The S.E for each of the three cases was kept from 2 mrad to 4 mrad, and numerical analysis was conducted by applying the algorithm given in Fig. 3. The algorithm mentioned in Fig. 3 was used in performing the numerical simulation to estimate the conversion efficiency of the solar thermochemical reactor. This algorithm is a combination of the optical system (Solar concentrated system) and a thermochemical system (STCR). The optical system is designed, and a solar flux profile is generated using SolTrace software and the flux profile is used to generate the temperature in the STCR to initiate the redox reactions through the Computational Fluid Dynamics (CFD) analysis method. This combination of SolTrace and CFD method integration allows us to carry out the redox reactions at a specified temperature and control the reaction dynamics to obtain the simulation results.

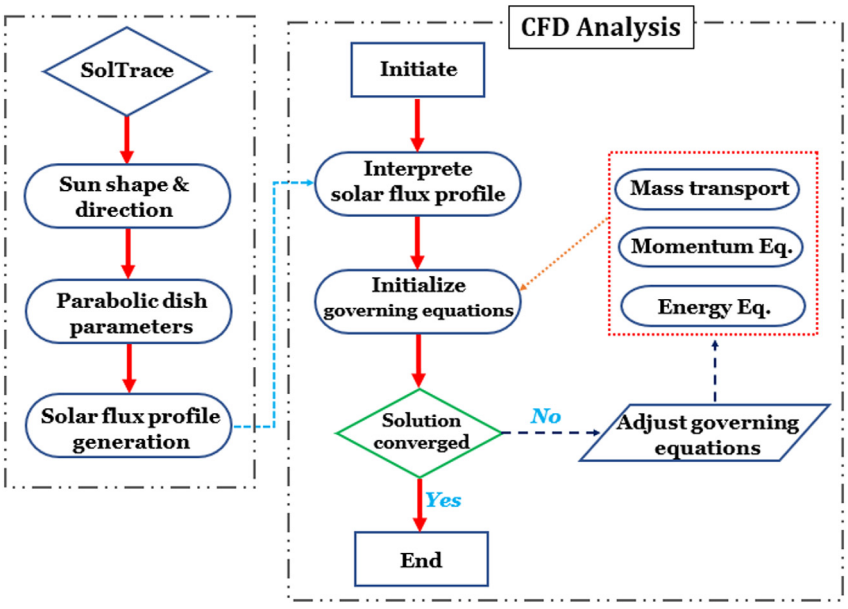


**Fig. 3.** Solution algorithm for the analysis.

**Table 1**
Material properties and expressions (Furler and Steinfeld, 2015).

| Constitutes | Characteristics | Value | T (K) |
|---|---|---|---|
| RPC-$CeO_2$ | Density (kg/m$^3$) | 7220 | 298 |
| | Specific heat (J/kg-K) | $-(0.0001271)\,T^2+(0.2697656)\,T+299.8695684$<br>444.27 | 280–1100<br>>1100 |
| | Thermal conductivity (W/m-K)<br>Absorption coefficient (m$^{-1}$) | $-(1.72)\,10^{-9}T^3+(1.12)\,10^{-5}T^2-(0.024)T+17.80$<br>$(1-\{-6\,(10^{-5}T+0.411)\}\times 497.8)$ | 280–2000<br>300–2500 |
| | Scattering coefficient (m$^{-1}$) | $-6\,\{(10^{-5}T+0.411)\,497.8\}$ | 300–2500 |
| QZ glass | Density (kg/m$^3$) | 2500 | 298 |
| | Specific heat (J mol$^{-1}$-K$^{-1}$) | $-0.0001T^2+0.1791T-0.173$<br>$0.0072T+61.717$ | 273–847<br>847–2000 |
| | Thermal conductivity (W m$^{-1}$ -K$^{-1}$) | $1.18+(3.14)10^{-3}T+\frac{17966}{T^2}$ | 273–2000 |

This particular methodology is crucial in designing an efficient solar thermochemical reactor at the lab-scale, which can further be scaled up to operate at the pilot scale.

The solar flux profile is generated by the MCRT method using SolTrace software. ANSYS Fluent v16.0 was used to generate the reactor cavity temperature and flux distribution. For numerical analysis, the energy equations were solved using the Discrete Ordinates thermal irradiation model. Table 1 shows the simulation's thermophysical properties of RPC.

### 2.1. Numerical techniques

The numerical simulations are based on the following mentioned set of equations (Reich et al., 2015; Haussener et al., 2009):

(1) **Conservation of mass**

$$\frac{\partial \rho}{\partial t}+\nabla.(\rho\vec{v})=0 \tag{4}$$

(2) **Conservation of momentum**

$$\frac{\partial}{\partial t}(\rho\vec{v})+\nabla.(\rho\vec{v}\vec{v})=-\nabla \mathrm{p}+\nabla.(\mu\nabla\vec{v})+S_p \tag{5}$$

In the above given Eq. (2), the Sp denotes the fluid pressure drop source term and P and $\mu$ designate the fluid pressure drop and dynamic viscosity, respectively. The pressure drop source term is calculated as (Wu et al., 2011a):

$$S_p=-\left(\frac{1039-1002\phi}{d_s^2}\right)\mu u-\left(\frac{0.513\phi^{-5.739}}{d_s^2}\right)\rho_f u^2;$$
$$0.66\le \emptyset \le 0.93 \tag{6}$$

In the above given Eq. (16), $\phi$ and $d_s$ denote material porosity and mean cell size, respectively. The flow is given at the entrance in the porous structure, the gradient is set to 0 at the fluid outlet.
Ar entrance of conduit: u = $u_0$, v = 0
At exit of conduit: $\frac{\partial u}{\partial x}=\frac{\partial u}{\partial y}=\frac{\partial v}{\partial x}=\frac{\partial v}{\partial y}=0$

(3) **Energy equation**

$$\frac{\partial}{\partial t}(\rho h-p)+\nabla.[\vec{v}(\rho h)]=\nabla.\left(\lambda_{eff,f}\nabla \mathrm{T}\right)+S_h \tag{7}$$

In the above-mentioned mathematical expression, $S_h$ is known as a source term which allows heat transport from the solid to the fluid phase.

$$S_h=h_v(T_s-T_f) \tag{8}$$

where $h_v$ (W/m$^3$ k) is known as the volumetric convective heat transport coefficient and it can be considered using the

correlation given by (Wu et al., 2011a)

$$h_v = \frac{\lambda_f \left(32.504\phi^{0.38} - 109.94\phi^{1.38} + 166.65\phi^{2.38} - 86.98\phi^{3.38}\right) Re^{0.438}}{d_s^2}; \quad \{0.66 \le \phi \le 0.93 \; and \; 70 \le Re \; 800\} \tag{9}$$

The Eq. (10) is modified as follows to be used in the solid

$$\frac{\partial}{\partial t}(\rho h) = \nabla.\left(\lambda_{eff,f} \nabla \mathrm{T}\right) + S_s \tag{10}$$

$\lambda_{eff,f}$ and $\lambda_{eff,s}$ denote the effective thermal conductivity and Ss known as the volumetric heat source term. These entities can be calculated using the following given correlations (Wu, 2015);

$$\lambda_{eff,f} = \phi\lambda_f \tag{11}$$

$$\lambda_{eff,s} = \lambda_s(1-\phi) \tag{12}$$

The source term includes the radiative ($S_{rad}$), convective ($S_{conv,s}$) as well as heat dissipation ($S_w$).

$$S_s = S_{conv,s} + S_{rad} + S_w \tag{13}$$

***i. Source term for thermal transport***

The heat transport source term is given to estimate the amount of heat exchange between the solid-to-fluid phase,

$$S_{conv,s} = -S_{conv,f} = -h_v(T_s - T_f) \tag{14}$$

***ii. Wall heat dissipation source term***

The solar thermochemical reactor operates at high temperatures thus the heat dissipation consideration becomes crucial and it can be calculated by the following equation,

$$S_w = -\varepsilon_w \sigma \left(T_s^4 - T_0^4\right) \tag{15}$$

***iii. Discrete Ordinates irradiative transfer model***

The energy and radiative transfer equation through the porous media can be written as follow (Keshtkar and Gandjalikhan Nassab, 2009);

***(a) Fluid energy equation***

$$-\varphi\rho_f u_f c_f \frac{\partial T_f}{\partial x} - (1-\varphi)hA(T_f - T_s) + \varphi Q(y)\delta(x) + \varphi k_f \left(\frac{\partial^2 T_f}{\partial x^2} + \frac{\partial^2 T_f}{\partial y^2}\right) = 0 \tag{16}$$

***(b) Solid energy equation***

$$\nabla.q + (1-\varphi)hA(T_s - T_f) - (1-\varphi)k_s\left(\frac{\partial^2 T_s}{\partial x^2} + \frac{\partial^2 T_s}{\partial y^2}\right) = 0 \tag{17}$$

The thermal conduction via. gas can be easily neglected because of the marginal thermal conductivity of the inert gas.

***iv. Radiation transport equation***

$$\frac{d\boldsymbol{I}_\lambda(\vec{\boldsymbol{r}},\vec{\boldsymbol{s}})}{\boldsymbol{ds}} + (\boldsymbol{k}_\lambda + \boldsymbol{\sigma}_\lambda)\boldsymbol{I}_\lambda(\vec{\boldsymbol{r}},\vec{\boldsymbol{s}}) = \boldsymbol{\varepsilon}_\lambda \boldsymbol{I}_{\boldsymbol{b},\lambda} + \frac{\boldsymbol{\sigma}_\lambda}{\boldsymbol{4\pi}} \int_0^{4\pi} \boldsymbol{I}_\lambda(\vec{\boldsymbol{r}},\vec{\boldsymbol{s}}')\boldsymbol{\phi}_\lambda(\vec{\boldsymbol{s}} \to \vec{\boldsymbol{s}}')\boldsymbol{d\Omega}' \tag{18}$$

The radiative heat flux (q) in the solid region of porous media is computed by the equation given below;

$$q = \int_{4\pi} I(r,\hat{s})\hat{s}d\Omega \tag{19}$$

In the DO irradiation model, a limited number of discrete angles are solved through RTE. These angles are in connotation with the vector quantity denoted by $\vec{s}$. The DO irradiative model solves the same quantity of conservation equations for all possible directions ($\vec{s}$). The RTE equation taken into account by the DO irradiative model is given in Eq. (19).

(4) **Mass transfer**

The mass transfer equations can be written as follows:

$$\frac{\partial(\boldsymbol{\rho_f Y_i})}{\partial \boldsymbol{t}} + \nabla.(\boldsymbol{\rho_f v Y_i}) = \boldsymbol{0} \tag{20}$$

$$\frac{\partial(\boldsymbol{\chi\rho_f Y_{O_2}})}{\partial \boldsymbol{t}} + \nabla.(\boldsymbol{\chi\rho_f v Y_{O_2}}) = \boldsymbol{S_{m,O_2}} \tag{21}$$

$$\frac{dm_p}{dt} = \dot{m}_p \tag{22}$$

where Yi, $\dot{m}_p$ and $S_{m,O_2}$ are known as component concentration, particle mass transfer rate and mass source term, respectively.

The oxygen evolution rate equates to the rate of particle mass transfer. Therefore, the particle mass changed fraction defines the reaction rate as shown (Ishida et al., 2014);

$$\frac{dx}{dt} = k_{red}(1-x) \tag{23}$$

$$x = \frac{m - m_i}{m_f - m_i} \tag{24}$$

where, $k_{red}$ is the reduction rate co-efficient and m, $m_i$ and $m_f$ denote the particle's time-dependent starting, and terminal masses and the value of m can be calculated by Eq. (25)

$$m = m_i - \delta n_{CeO_2}\frac{M_{O_2}}{2} \tag{25}$$

Thus, the reaction rate can be given as Eqs. (26) & (27);

$$\frac{dm_p}{dt} = (m_f - m_i)k_{red}\left(1 + \frac{\delta\frac{m_i}{M_{CeO_2}}M_{O_2}}{2(m_f - m_i)}\right) \tag{26}$$

$$\frac{\delta}{(0.35-\delta)} = 8700\left(P_{O_2}bar\right)^{-0.217}\exp\left(\frac{-195.6 \text{ kJ} - \text{mol}^{-1}}{RT}\right) \tag{27}$$

In the above-given equation, $\delta$ denotes the non-stoichiometric coefficient and depends on the reaction's operational temperature and $O_2$ partial pressure (Bulfin et al., 2013). The oxygen partial pressure can be calculated from Eq. (28);

$$P_{O_2} = (M_{O_2} \times P_{tot}) \tag{28}$$

### 2.2. SolTrace modelling

The optical modelling and analysis are done using the MCRT-based SolTrace software (Wendelin, 2003). The SolTrace modelling has been executed in the following steps:

(1) **Parameters selection**

The angular intensity pattern on the area is described as a sun shape. The SolTrace software provides the user with three options to select the sun-shape as Gaussian, pillbox, or user-defined profiles. Given the accuracy of the pillbox profile, it has been adopted as the utmost suitable pick for optical simulation in SolTrace. In this sun-shape distribution profile, the incidence of solar irradiation stays steady but the collimated rays subtended with 4.65 mrad S.E (Chen et al., 2016; Johnston, 1998). A DNI value of 998 W/m$^2$ has been adopted to normalize the solar flux in the solar ray tracing technique (Hasuike et al., 2006).

(2) **CSP system properties**

A CSP system's concentration performance is limited by optical imperfections. A CSP system's vast surface area causes errors to follow the Gaussian distribution. SolTrace enables users to select the appropriate study-specific error type, such as Pillbox or Gaussian. The specularity errors occur when the error scale for surface flaws is less than the solar spectrum (Cooper and Steinfeld, 2011; Huang and Han, 2012). The tracking inaccuracy is caused by the optical system's imperfect placement. The overall error can be represented by the following Eq. (29).

$$\sigma^2 = \sigma^2{}_{specularity} + \sigma^2{}_{slope} + \sigma^2{}_{shape} + \sigma^2{}_{tracking} \cong \sigma^2{}_{slope,effective} \tag{29}$$

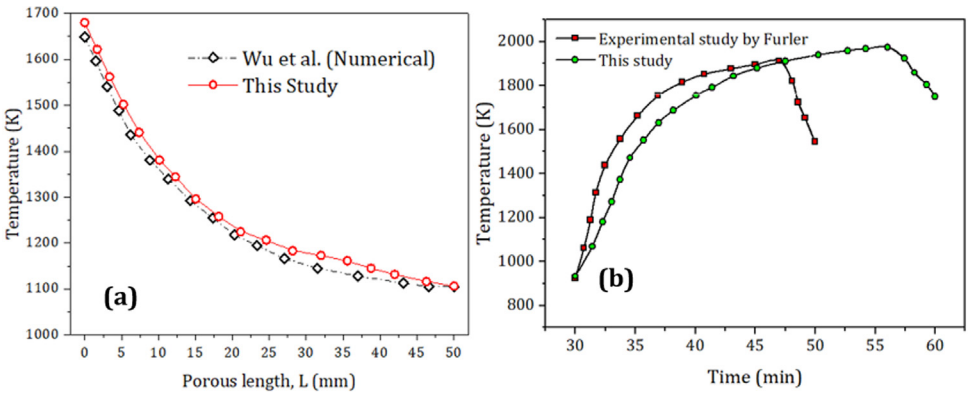


**Fig. 4.** (a) Fluid phase temperature validation against Wu et al. (2011b) and (b) Fluid phase temperature distribution after the pre-heating stage validated against Furler and Steinfeld (2015) in transient analysis.

Specularity errors consist of mirrored and tracking errors (Luo et al., 2014). The $\sigma_{specularity}$ value of 0.2 mrad has been adopted in this optical analysis (Binotti et al., 2017).

The optical error can be estimated by Eq. (30) as given below (Wendelin et al., 2013).

$$\sigma_{optical} = \sqrt{\left(4\sigma^2{}_{slope} + \sigma^2{}_{specularity}\right)} \tag{30}$$

For a typical solar concentrator, the S.E component lies within 2 to 4 mrad (Johnston, 1995; März et al., 2011).

The chemical performance of the solar thermochemical reactor is estimated by the solar-to-fuel conversion efficiency estimating by using the following mentioned Eq. (31).

$$\eta_{solar-to-fuel} = \frac{\dot{n}_{fuel} HHV_{fuel}}{Q_{input-solar-energy}} \tag{31}$$

where $\dot{n}_{fuel}$ denotes the rate of $H_2$ production, $HHV_{fuel}$ represents the higher heating value of $H_2$ and $Q_{input-solar-energy}$ is the solar energy required to operate the reduction step.

(3) **Profile generation**

Two components of optical systems are reflectors and receivers. Thus, the optical system in SolTrace was created in two stages, Dish and Target. The stages are arranged in a way that the solar irradiation strikes first on the dish and then on the target. The optical and surface properties, characteristics, element position, and orientation is provided according to the analysis requirement.

### 2.3. Numerical implementation

The numerical simulation was carried out using SolTrace which traces solar ray paths using the MCRT technique. MCRT uniformly distributes solar power by dividing it into a larger number of rays determined by the sun shape and S.E (Shuai et al., 2008). The interaction between the rays and the reactor cavity is influenced by transmissivity, reflectivity and absorptivity. The SolTrace results were validated against Lee's study and further used as radiative flux boundary conditions on the quartz glass window. ANSYS Fluent v16.2 solver was utilized to compute the conservation equations by the finite volume technique with a tetragonal/hexagonal unstructured mesh having a 0.5 mm element size.

The DO irradiation model was employed to calculate the RTE equation in the solar thermochemical reactor cavity. Steady-state simulation with COUPLED first-order upwind for discrete ordinates and second-order for energy calculation was implemented. The boundary conditions applied in the numerical simulation have been mentioned in Table 2.

**Table 2**
Boundary conditions.

| Surface | Boundary conditions |
|---|---|
| Inlets | $v_{inlet} = \frac{\overset{*}{v}}{Ac_{inlet}}$; $T_{inlet} = T_{initial}$ |
| Outlet | $P_{out} = P_{atm}$ |
| Inner surface | $k_q \frac{\partial T}{\partial n} = S_{E,rad} + h_q \Delta T$; $\varepsilon = 0.08, \tau = 0.86$ |
| Insulation wall | $k_s \frac{\partial T}{\partial n} = \Delta q_r + h_s \Delta T$; $\varepsilon = 0.28, \tau = 0$ |
| Quartz window | $T_{aperture} = T_{initial}$; $\varepsilon = 0.08, \tau = 0.86$ |
| Other surfaces | $\frac{\partial T}{\partial n} = 0$ |

### 2.4. CFD-SolTrace model validation

The fluid-phase temperature in the porous region has been validated against Wu et al. as demonstrated in Fig. 4. Wu et al. focused on the thermal transport modelling of a volumetric foam reactor having a pore size of 0.5–3 mm. The present modelling of STCR is also focused on thermal transport modelling coupled with species transport modelling. Hence the thermal transport result of the present study is validated against the Wu et al. results. The findings of the presented CFD analysis are in very good conformity with the referenced study. It was also seen that the attained results are in high concordance with other research reported. The outcomes of this study can also be validated against some other studies such as Cooper and Steinfeld (2011), Huang and Han (2012), Luo et al. (2014) and Loni et al. (2016).

## 3. Results and analysis

### 3.1. The sensitivity of flux distribution at the STCR cavity aperture

The thermal analysis examined two STCR cavity configurations (Fig. 1). Semi-transparent quartz glass allows solar irradiation into the cavity. Geometry modification improves radiation dispersion and achieves the highest temperature at low solar flux in the porous RPC region. The length of the cylindrical section is kept at 80 mm while the hemispherical section has a radius of 20 mm for the first model. In the second model, the length of the conical frustum section is 70 mm and the hemispherical section radius is 30 mm. The aperture radius of both models was taken as 20 mm with a porous catalyst region thickness of 20 mm.

Fig. 5 illustrates the solar flux pattern for all three situations as computed by the SolTrace software. The focal distance (f) for 1st,

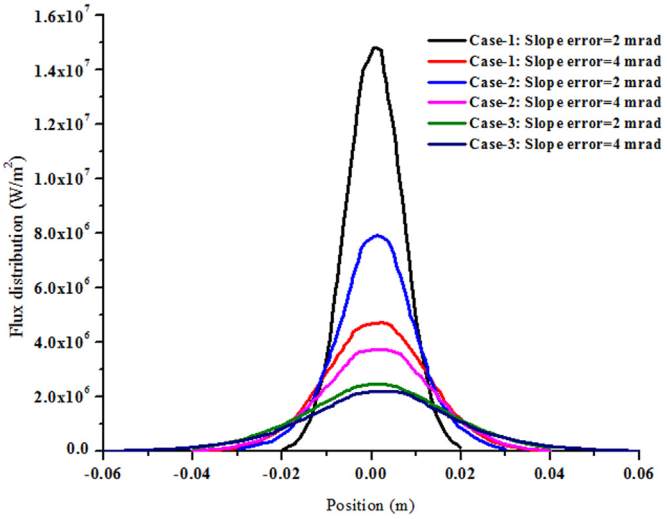


**Fig. 5.** Concentrated solar flux distribution.

2nd and 3rd cases was kept at 0.9803 m, 0.9703 m, and 0.9603 m, respectively. It was readily apparent from the graph that 1st case with 2 mrad S.E yields the peak value of solar flux at the cavity aperture. In 2nd case of 2 mrad S.E, the flux value is relatively low. The flux value for case-1 with 4 mrad S.E is substantially higher than the attained flux value for case-2 with both S.E values. These flux profiles were later used as a UDF profile to generate the solar flux in the solar reactor on the porous walls to generate the required temperature for carrying $H_2O/CO_2$ splitting redox reactions.

### 3.2. Temperature distribution

Optical and geometrical optimization achieves consistent temperature and distribution of solar flux on the STCR wall for $H_2O/CO_2$ splitting. The temperature contours for STCR – 1 & 2 have been shown in Fig. 6(1) & (2), respectively. 1st model of STCR cavity for 4 mrad milliradians S.E has a more consistent and higher temperature distribution than 2 mrad S.E. Cases 1, 2, and 3 with 2 mrad S.E. yield elevated values of solar flux, whereas 4 mrad S.E. yield the higher temperature distribution in the porous matrix. In case 1, the incidence of solar flux was not uniformly distributed throughout the porous zone, resulting in a lower temperature than anticipated. Meanwhile, with a 4-mrad S.E, the solar flux reaches the STCR and creates uniform flux distribution, leading to larger temperature distribution than a 2-mrad S.E. The geometrical aspect of STCR cavity design plays a significant role in uniform flux and temperature distribution as represented in the temperature contours. The 2nd model poses the advantage of having conical frustum at the entrance which allows the more uniform distribution of collimated rays resulting in yielding a higher temperature at the porous region as compared to the 1st model.

#### 3.2.1. Radial direction

The RPC zone is where redox reactions take place to produce $H_2$ gas. Thus, the investigation of radial temperature distribution in the catalyst region is a crucial factor to optimize the RPC thickness in the solar reactor. The radial temperature profile in the porous media for the 1st, 2nd and 3rd cases in which the focal point was considered at ($x = 0, -10$ and $-20$ mm) has been shown in Fig. 7(a) and (b) for model-1 and 2, respectively. Case-2 with 4 mrad S.E produces the maximum temperature zone in a 20 mm porous medium. Both models exhibit uniform radial

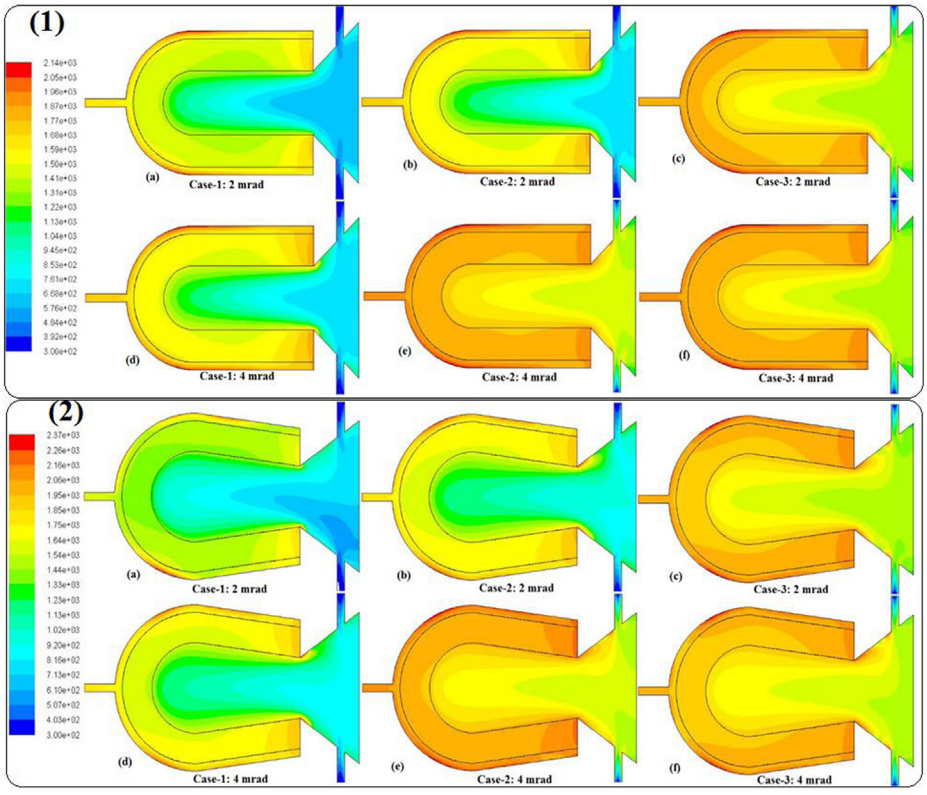


**Fig. 6.** Fluid phase temperature contours **(1)** STCR – 1 **(2)** STCR – 2, for all three cases.

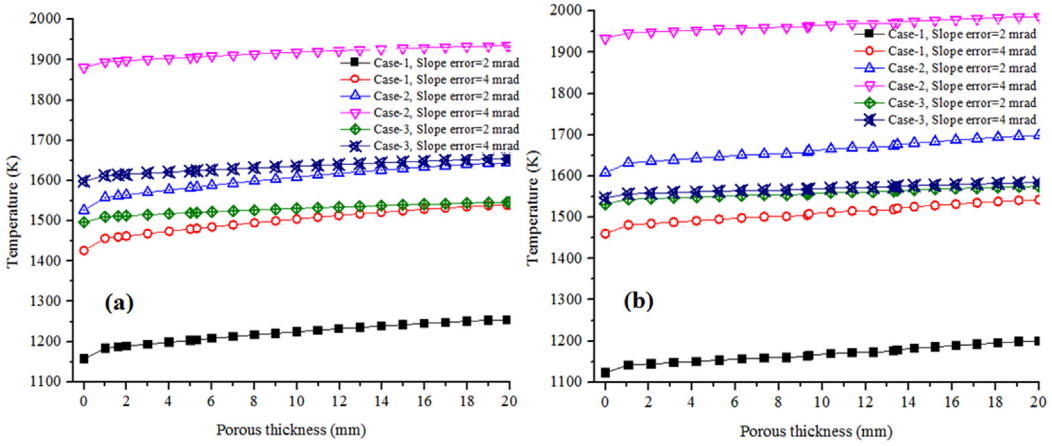


**Fig. 7.** Radial temperature distribution (a) STCR – 1 and (b) STCR – 2.

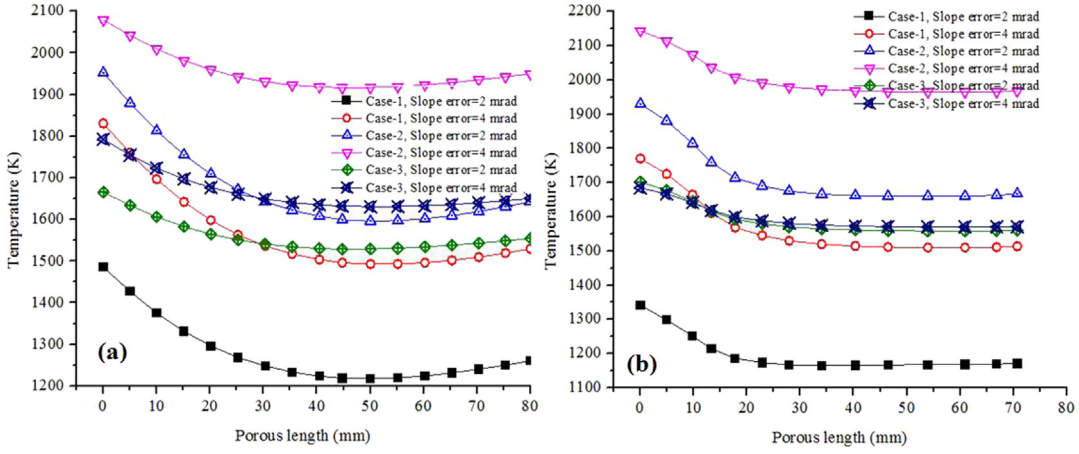


**Fig. 8.** Fluid phase axial temperature distribution (a) Model – 1 and (b) Model – 2.

temperature distribution, although model-2 yields 52 K higher than model-1.

If the flux is uniformly distributed in the porous region, a higher, more uniform temperature could be produced at an increased inert gas velocity. Statistics reveal that cavity geometry affects radial temperature distribution. Model-2 offers more uniform and significantly increased radial temperature distribution than the model-1. The frustum section evenly distributes flux and results in increasing radial temperature in the porous structure. The influence of S. E on radial temperature is small for both S.Es. Considering that the focus point is at 20 mm within the STCR, the solar flux could enter with little dispersion, resulting in uniform flux distribution and consistent temperature distribution in the catalyst zone.

### 3.2.2. Axial direction

The axial temperature profile is critical for determining the optimal RPC reactive surface area of the STCR. The axial temperature distribution in the catalyst section should be addressed. Since the cavity's cylindrical and conical frustum are 80 and 70 mm, respectively. Thus, the axial temperature distribution for this area was assessed, and the semi-circular section of the solar reactor is included in the assessment of the temperature profile along the solar reactor centreline. The fluid phase temperature profile of the porous media in the axial direction has been plotted in Fig. 8(a) for model-1 and (b) for model-2. It is reported that case-2 ($x = -10$ mm) exhibits higher temperature trends among all three cases in both models. However, a comparative analysis of both models reveals that model – 2 for case-2 with 4 mrad S.E yield 328.8 K higher mean temperature as compared to model-1 while subjected to similar conditions. It was also seen that in terms of consistency of temperature profile along the longitudinal axis in a porous material, from $x = 0$ to $x = -80$ mm, model-2 offers a significant advantage over model-1. The uniformity in the temperature distribution throughout the length is a result due to the geometric effects.

### 3.2.3. STCR length

The study of fluid-phase reactor temperature is required in order to optimize the fluid–phase reactor temperature in the solar thermochemical reactor for redox reaction. When it is necessary to switch between two parts of a continuing process, improved temperature control is advantageous.

Through the semi-transparent glass, concentrated solar radiation enters the solar reactor and the temperature of the STCR cavity started to rise by means of convection (heated inert gas) and radiation. Fig. 9(a) and (b) presents the temperature profile of the fluid phase along the longitudinal axis in the STCR for model-1 and 2, respectively. Given the stipulation that the point of focus is at the $x = 0$ which results in the scattering of the collimated rays starts at this point. It is observed in Fig. 9(a) and (b) that case-2 with 4 mrad S.E yields the highest reactor temperature for both models. However, model-1 reached 21.28 K higher mean temperature as compared to model-2. In terms of uniformity throughout the entire length of the solar thermochemical reactor, both models perform equally well.

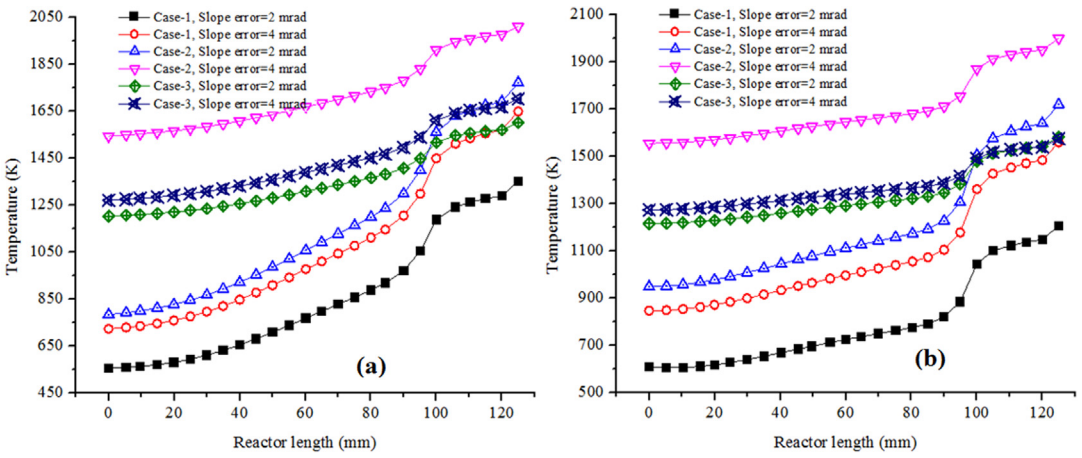


**Fig. 9.** Reactor temperature (a) Model-1 and (b) Model-2.

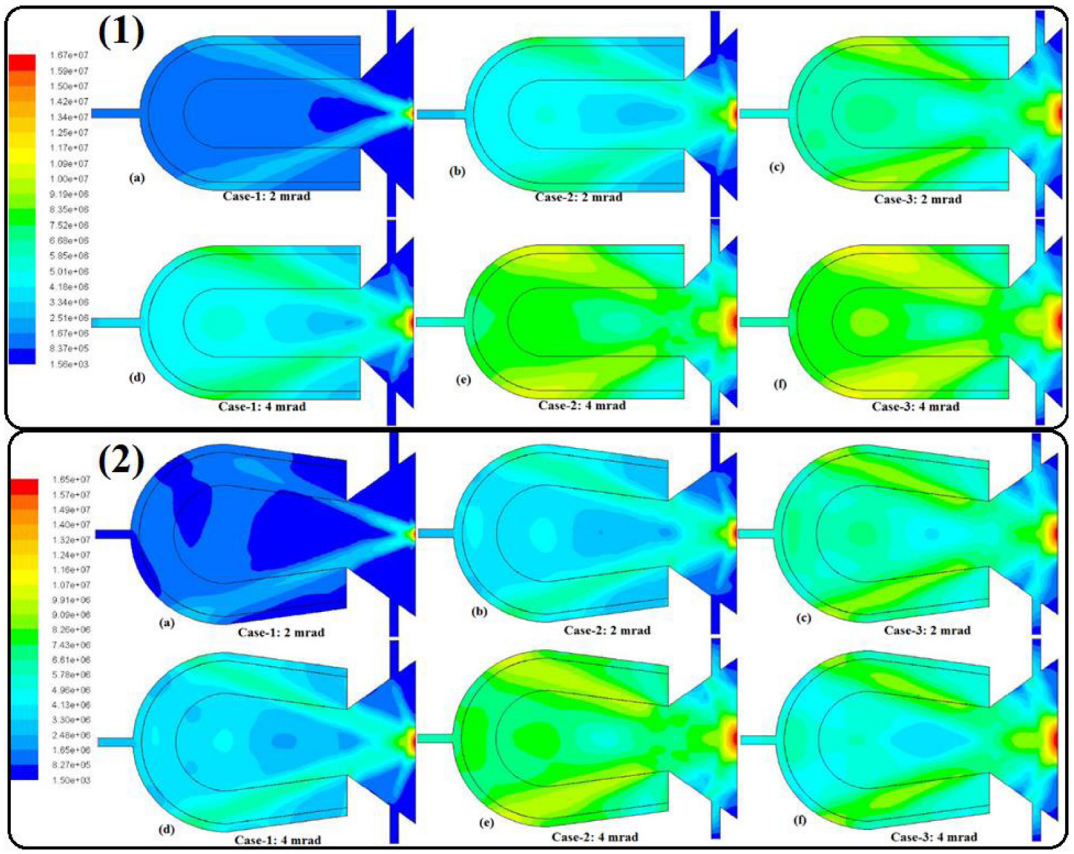


**Fig. 10.** Flux distribution contours for model-1 for all three cases with both S. Es.

### 3.3. Flux distribution in the porous region

The optical interpretation is based on the STCR flux distribution. Fig. 10(1) and (2) for model-1 and model-2 illustrate flux distribution contours for all three conditions. The flux distribution contours indicate that focal distance is key to uniform solar flux dispersion in porous regions. When the point of focus is within the cavity, rays scatter better, resulting in uniform flux and temperature distribution for both models. In both Fig. 10(1) and (2), the solar flux dispersion is reported to be far more consistent and higher in magnitude for 4 mrad S.E. However, the effect was only apparent if the point of focus was within the solar reactor *i.e.* in case-2 and case-3. Another important observation was that when the point of focus was at the aperture of the solar reactor in the model-1, it achieved a higher flux magnitude and better uniformity but as the focal point slides further inside in cavity, model-2 becomes a better choice for achieving the uniform flux as compared to model-1.

Fig. 11 shows that the solar flux dispersion in the solar reactor depends on the focal point shift and the cavity shape. It is evident that the flux distribution in the STCR cavity also depends on the S.E. The flux distribution in model-1 and model-2 was seen to be greater for 4 mrad S.E compared to 2 mrad for case-1. However, the flux distribution in mode-1 is comparatively more sophisticated than model-2. It can be also seen in both Figures that the model-1 STCR cavity shape provides more uniform flux

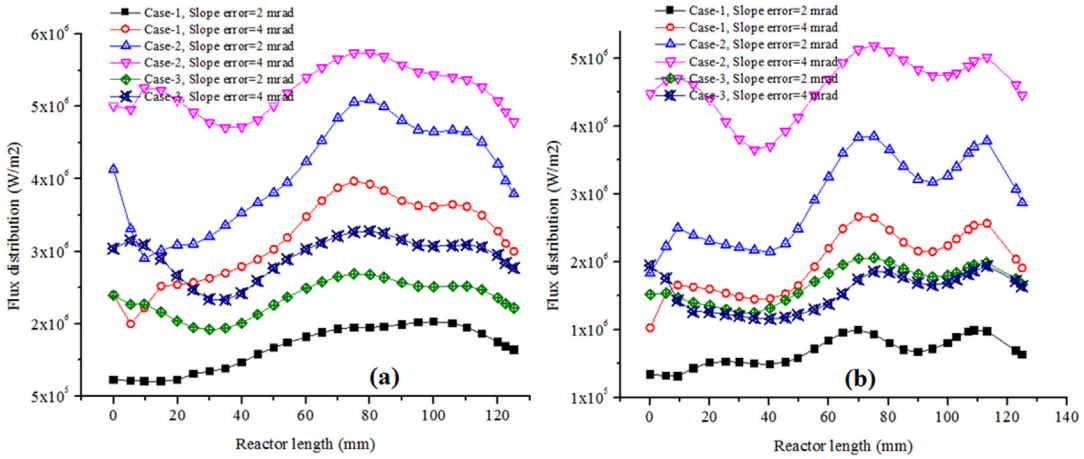


**Fig. 11.** Solar flux profiles in the solar reactor for (a) model-1 and (b) model-2.

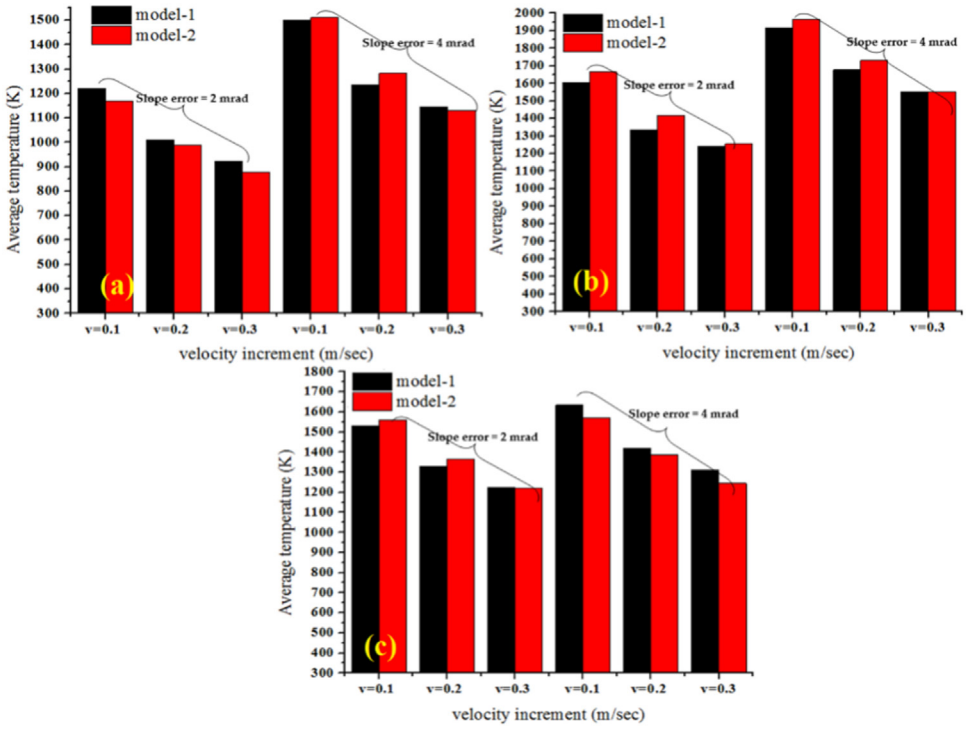


**Fig. 12.** Average fluid phase temperature in radial direction wrt. Inert gas velocity for S.E 2 and 4 mrad.

distribution as compared to model-2. As the point of focus moves 10 mm within the STCR in the second case, the flux distribution for both models and for both S.E increase significantly. It is also seen that model-1 with 4 mrad S.E offers more unvarying flux distribution as compared to model-2. In the third case, as the point of focus was located at 20 mm further within the STCR, the solar flux profile in the solar reactor reduces drastically in comparison to the 2nd case but still yields greater magnitude than in the 1st case. The magnitude of flux in model-1 is higher for 4 mrad S.E while in model-2, the impact of S.E does not show much significance.

### 3.4. Influence of optical error

Concentrators may have optical imperfections, which can affect the solar flux profile. The optical errors are mainly caused by the S. Es and its value varies between 2 to 4 mrad. The dissimilarity in solar flux distribution profiles caused by S. Es can be seen in Fig. 5. It can be seen quite well that the magnitude of the solar flux decreases with the increase in solar error value. However, the distribution of flux distribution for 4 mrad S.E is higher than for 2 mrad S.E. The extreme values of solar flux 15, 7 and 2 MW/m$^2$ are obtained for case-1, 2 and 3 with 2 mrad S.E, respectively. The statistical influence of S.Es on average fluid phase temperature in the porous media for both models by taking the effects of inert gas velocity into account have been discussed in Fig. 12 fluid temperature in the radial direction, Fig. 13 fluid temperature in the axial direction and Fig. 14 for fluid temperature in reactor along the centreline.

The average fluid phase temperature in the porous region for all three cases has been plotted in Fig. 12. When the inert gas velocity was 0.1 m/s at the inlet and the 2 mrad S.E, the avg. fluid temperature in the RPC region reached 1220 K and 1168 K for model-1 and 2, correspondingly. However, the avg. the temperature reached the value of 1500 K and 1510 K for 4 mrad S. E with the same velocity as shown in Fig. 12(a) for case-1. This

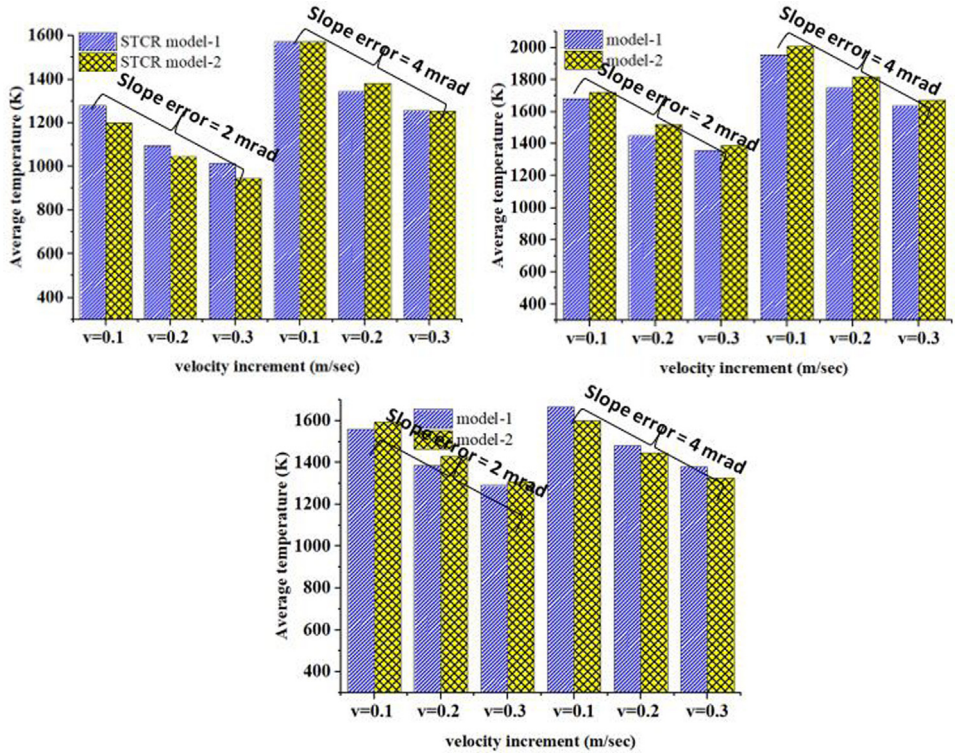


**Fig. 13.** Average fluid phase temperature in axial direction wrt. Inert gas velocity for 2 and 4 mrad S.E.

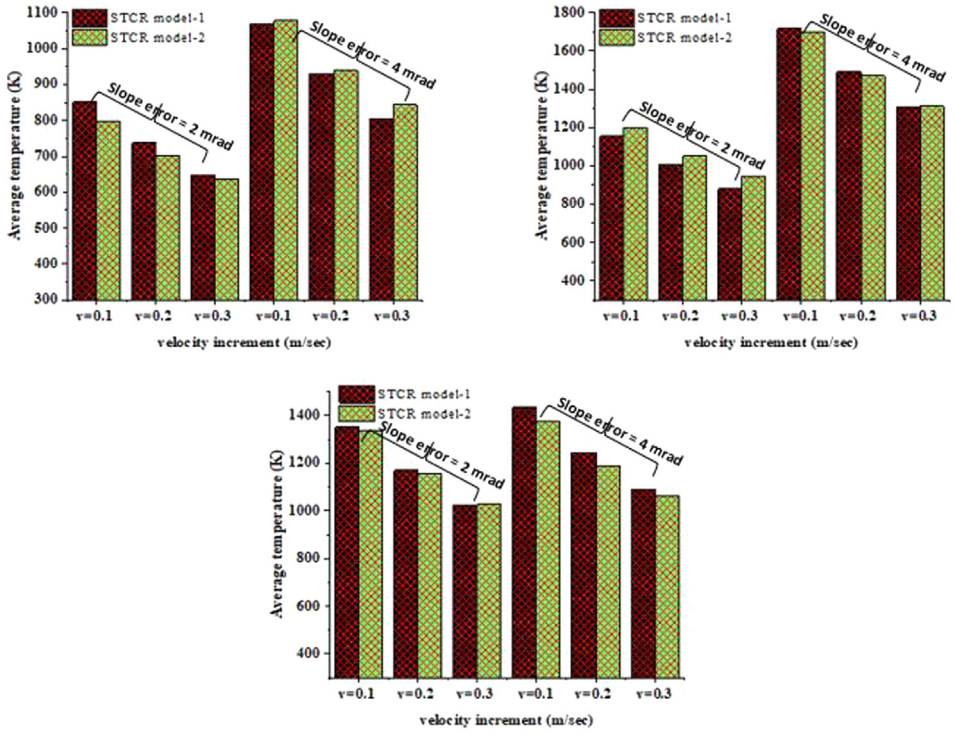


**Fig. 14.** Average temperature in STCR wrt. Inert gas velocity for S.E 2 and 4 mrad.

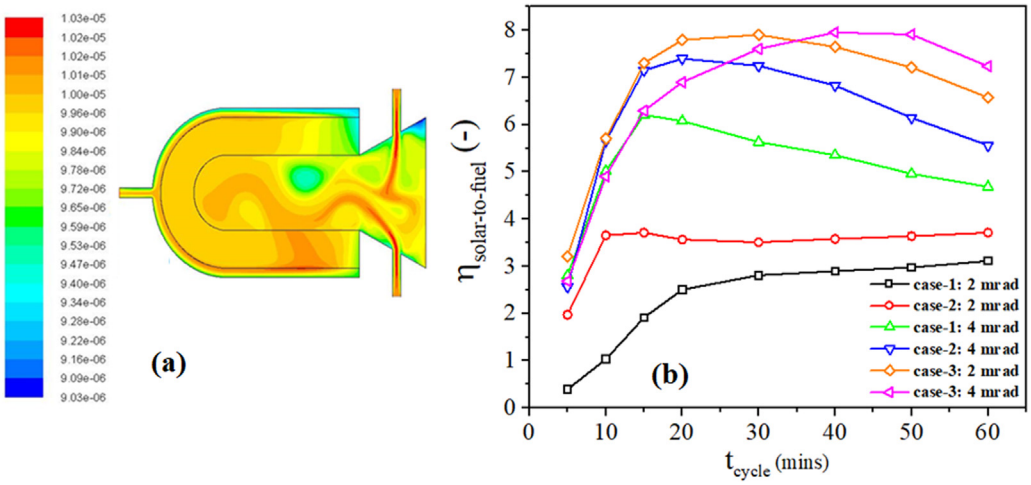


**Fig. 15.** (a) Oxygen evolution contour; (b) Solar-to-fuel conversion efficiency for model-1.

rise of 280 K and 342 K in avg. temperature for model-1 & 2, correspondingly signifies the importance of S.E. It also should be noted that the increment in inert gas velocity from 0.1 m/s to 0.3 m/s causes in decrease avg. temperature by 296 K and 354 K for model-1 and 291 K, 378 K for model-2 for 2 mrad and 4 mrad S.E, respectively.

In the 2nd case where the focal point of focus is 10 mm (x = −10 mm) inside the STCR, the avg. fluid temperatures for both models have been exhibited in Fig. 12(b). Further, it was observed that the avg. temperature reached much higher than in case-1. Statistically, for the inert gas velocity of 0.1 m/s, the avg. temperature for model-1 goes up to 1604 K and for model-2 goes up to 1664 K for 2 mrad S.E. However, if S.E. is set to be 4 mrad, the avg. temperature goes up to 1917 K and 1966 K for model-1 and model-2, respectively. Whereas shifting of point of focus 20 mm inside the cavity (at −20 mm) reduces the avg. temperature for both models with both S. Es is shown in Fig. 12(c). The model-1 and model-2 with 2 mrad S.E yield 1528 K and 1560 K and with 4 mrad S.E yield 1634 K and 1571 K of avg. temperature, respectively. Thus, it is statistically stipulated that model-2 provides the best-case scenario to achieve the highest avg. fluid temperature with 4 mrad S.E and 2nd case, when the point of focus is 10 mm within the solar reactor, is the best choice among all three cases.

The avg. fluid temperature distribution in axial direction has been demonstrated in Fig. 13(a), (b) & (c) for case-1, 2 and 3. In the first case as shown in Fig. 13(a), the avg. temperature goes up to 1280 K for model-1 and 1200 K for model-2 at 2 mrad and 1570 K for model-1 and 1572 K for model-2 at 4 mrad S.E at 0.1 m/s inert gas velocity. By shifting the focal point 10 mm inside the cavity (2nd case) as exhibited in Fig. 13(b), the avg. temperature gets higher and reached up to 1670 K and 1722 K for model-1 & 2, correspondingly at 2 mrad and 1955 K and 2008 K for model-1 & 2, correspondingly at 4 mrad S.E. While in case-3 as shown in Fig. 13(c), the avg. temperature for model-1 & 2 reached up to 1561 K and 1594 K, respectively at 2 mrad and 1667 K and 1599 K, respectively at 4 mrad. It is clear that the distribution of avg. fluid temperature in the axial direction is highest for case-2 at 4 mrad and model-2 is the best suitable choice in this scenario.

The avg. temperature of the reactor along the centreline for all three cases have been plotted in Fig. 14(a), (b) & (c). In the 1st case as demonstrated in Fig. 14(a) the avg. temperature goes up to 852 K and 798 K for model-1 & 2, correspondingly for 2 mrad and 1070 K and 1079 K for model-1 & 2, correspondingly at 4 mrad S.E for 0.1 m/s fluid velocity. However, for case-2 the avg. reactor temperature for model-1 and model-2 reached up to 1156 K and 1201 K, respectively at 2 mrad and 1720 K and 1700 K for model-1 & 2, correspondingly at 4 mrad as illustrated in Fig. 14(b). However, in the 3rd case as shown in Fig. 14(c), the avg. reactor temperature goes up to 1353 K and 1335 K for model-1 and model-2 at 2 mrad and 1434 and 1374 for model-1 and model-2 for 4 mrad. Thus, model-1 reached the highest temperature at 4 mrad S.E in case-2 at 0.1 m/s fluid velocity.

### 3.5. Solar-to-fuel efficiency

The chemical performance of a solar thermochemical reactor is evaluated by estimating solar-to-fuel conversion efficiency as mentioned in Eq. (31). Solar-to-fuel conversion efficiency was evaluated as a function of solar flux distribution for all three cases considered in the presented study. The thickness of the porous region loaded with the reactive cerium oxide ($CeO_2$) was kept constant at 20 mm. The SolTrace-generated solar flux distribution profiles were subjected to produce the re-oxidation temperature ($T_L$) in the solar reactor *i.e.* 1250 K. The reduction stage was carried out for the period of 60 mins and the solar-to-fuel conversion efficiencies for all three considered cases were plotted as a function of oxygen evolution obtained from the simulation of the re-oxidation step.

The oxygen evolution contour is presented in Fig. 15(a) and it can be observed that when the reactive porous region of the solar reactor attains the re-oxidation temperature ($T_L$), the oxygen evolution becomes apparent. The solar-to-fuel conversion efficiency for all three cases for 60 min cycle period has been plotted in Fig. 15(b). The analysis shows that the highest value (7.95%) of the conversion efficiency was recorded for case 3 with 4 mrad S.E at the 40th min of the cycle. It can be deduced that case 3 with 4 mrad S.E offers the highest efficiency because it produces uniform solar flux distribution in the reactive porous region.

The previous studies in the literature have shown the solar thermochemical reactor efficiency for the cerium oxide-based thermochemical WS cycles to be less than 6% at the best possible operating conditions. However, the present study has proposed a solution to adjust the thermo-optical conditions to improve the distribution of temperature profile inside the reactor to sustain the continued operation of the thermochemical reactor which leads to better conversion efficiency, as demonstrated in Fig. 15.

## 4. Summary and conclusion

The thermal performance of the solar reactor is highly affected by the geometric configuration and optical parameters. The numerical research yielded the subsequent conclusions,

1. The STCR flux distribution is more uniform in model-1 for case-1 with 4 mrad S.E. Case-2 exhibits a more homogeneous flux distribution with 4 mrad S.E.
2. A high heat flux does not necessarily result in a high temperature if it is not evenly distributed within the cavity. Case-1 with 2 mrad S.E. yields 27% more solar flux, whereas Case-2 with 4 mrad S.E. produces a higher solar reactor temperature.
3. In cases 1 and 2, evenly distributed solar flux on the cavity walls produces a higher temperature in the porous zone. The flux distribution in case −3 loses homogeneity and magnitude. Thus it does not reach the same high temperature as case 1.
4. Model-2 for case-2 with 4 mrad S.E. produces the highest average STCR cavity temperatures in radial and axial directions. Model-1's centreline fluid temperature reached 1720 K in case-2 with 2 mrad S.E. Further, Model-2 produces greater homogeneity and higher radial catalyst temperature than model-1 in case-1 and case-2. In case 3, model-1 and model-2 offer similar radial catalyst temperatures.
5. The solar-to-fuel efficiency analysis shows that model-1 yields the highest efficiency of 7.95% for case-3 with 4 mrad S.E.

The foregoing findings offer geometrical and optical characteristics. The reactor cavity design and heat losses (convective and radiative) must be studied.

The optical analysis and cavity shape optimization are primary and important parts of the two-step $H_2O/CO_2$ splitting process of hydrogen and syngas production. It helps in choosing the perfect cavity shape which will allow to achieve the uniform solar flux distribution and maximum catalyst temperature. Further research will focus on the hydrogen production rate based on the optimized STCR cavity shape.

## Nomenclature

### Symbols

| | | | |
|---|---|---|---|
| A | Area ($m^2$) | b | Body |
| d | Collector aperture diameter (m) | conv | Convection |
| f | Focal length (m) | E | Energy |
| F | Force (N) | f | Fluid |
| Fs | Particle surface force (N) | $f_p$ | Fluid-particle interphase |
| g | Gravitational acceleration ($m/s^2$) | fs | Fluid-solid interphase |
| G | Incident radiative heat flux ($W/m^2$) | fuel | Chemical fuel |
| h | Collector height (m) | m | Mass |
| I | Radiative intensity ($W/m^2$) | p | Particles |
| k | Thermal conductivity (W/m-K) | $p_b$ | Particle black body |
| $k_a$ | Absorption coefficient (1/m) | q | Quartz glass |
| $k_{pa}$ | Particle absorption coefficient (1/m) | rad | Radiation |
| $k_{ps}$ | Particle scattering coefficient (1/m) | reac | Reaction |
| $k_{red}$ | Reduction rate coefficient | rim | Rim |
| $k_s$ | Scattering coefficient (1/m) | s | Solid |
| p | Pressure (Pa) | solar | Solar energy |
| $q_r$ | Re-radiation ($W/m^2$) | t | Total |
| Q | Heat amount (J) | th | Thermal |
| $Q_{a,p}$ | Absorption efficiency of particle | *i* | Initial |
| r | Reaction rate (mol/s) | *f* | Final |
| r$\pi$ | Parcel position | | |
| s | Distance in $\Omega$ direction | | |
| S | Source term | | |
| T | Temperature (K) | | |
| v | Velocity (m/s) | | |
| V | Volume ($m^3$) | | |
| Yi | Component concentration | | |
| $S_{m,O_2}$ | Mass source term | | |
| $S_p$ | Fluid pressure drop source term | | |
| $d_s$ | Mean cell size | | |
| $S_h$ | Convective heat transfer source term | | |
| $h_v$ | Volumetric convection heat transfer coefficient | | |
| Ss | Volumetric heat source term | | |

### Abbreviation

| | |
|---|---|
| CFD | Computational fluid dynamics |
| DEM | Discrete element method |
| DNI | Direct normal irradiance |
| DOM | Discrete ordinate method |
| HHV | Higher heating value |
| STCR | Solar thermochemical reactor |
| RPC | Reticulated porous ceramic |

### Greek Symbols

| | |
|---|---|
| $\beta$ | Extinction coefficient |
| $\delta$ | Non-stoichiometric coefficient |
| $\delta_p$ | Dirac delta function |
| $\eta$ | Efficiency |
| $\mu$ | Dynamic viscosity (Pa s) |
| $\rho$ | Density ($kg/m^3$) |
| $\sigma$ | Stefan–Boltzmann constant |
| $\psi$ | Angle (rad) |
| $\Omega$ | Solid angle |
| $\phi$ | Porosity |
| $\lambda_{eff}$ | Effective thermal conductivity |

## CRediT authorship contribution statement

**Jeet Prakash Sharma:** Conceptualization, Data curation, Writing – original draft. **Ravinder Kumar:** Conceptualization, Validation, Data curation, Writing – original draft. **Mohammad H. Ahmadi:** Supervision, Writing – original draft. **Azfarizal Mukhtar:** Validation, Supervision, Writing – review & editing. **Ahmad Shah Hizam Md Yasir:** Data curation, Writing – review & editing. **Mohsen Sharifpur:** Supervision, Funding. **Bulbul Ongar:** Conceptualization, Writing – review & editing. **Anara Yegzekova:** Supervision, Writing – review & editing.

## Declaration of competing interest

The authors declare that they have no known competing financial interests or personal relationships that could have appeared to influence the work reported in this paper.

## Data availability

No data was used for the research described in the article.

## References

Ardo, S. others, 2018. Pathways to electrochemical solar-hydrogen technologies. Energy Environ. Sci. 11 (10), 2768–2783. http://dx.doi.org/10.1039/c7ee03639f.

Barreto, G., Canhoto, P., 2017. Modelling of a stirling engine with parabolic dish for thermal to electric conversion of solar energy. Energy Convers. Manage. 132, 119–135. http://dx.doi.org/10.1016/j.enconman.2016.11.011.
Barreto, G., Canhoto, P., Collares-Pereira, M., 2018. Three-dimensional modelling and analysis of solar radiation absorption in porous volumetric receivers. Appl. Energy 215, 602–614. http://dx.doi.org/10.1016/j.apenergy.2018.02.065.
Bellos, E., Tzivanidis, C., 2019. A review of concentrating solar thermal collectors with and without nanofluids. J. Therm. Anal. Calorim. 135 (1), 763–786. http://dx.doi.org/10.1007/s10973-018-7183-1.
Bellos, E., Tzivanidis, C., Papadopoulos, A., 2019. Enhancing the performance of a linear fresnel reflector using nanofluids and internal finned absorber. J. Therm. Anal. Calorim. 135 (1), 237–255. http://dx.doi.org/10.1007/s10973-018-6989-1.
Binotti, M., Di Marcoberardino, G., Biassoni, M., Manzolini, G., 2017. Solar hydrogen production with cerium oxides thermochemical cycle. AIP Conf. Proc. 1850, http://dx.doi.org/10.1063/1.4984459.
Bork, A.H., Kubicek, M., Struzik, M., Rupp, J.L.M., Perovskite La0.6Sr, 2015. 0.4Cr1-xCoxO3-$\delta$ solid solutions for solar-thermochemical fuel production: Strategies to lower the operation temperature. J. Mater. Chem. A 3 (30), 15546–15557. http://dx.doi.org/10.1039/c5ta02519b.
Brendelberger, S., Holzemer-Zerhusen, P., Vega Puga, E., Roeb, M., Sattler, C., 2022. Study of a new receiver-reactor cavity system with multiple mobile redox units for solar thermochemical water splitting. Sol. Energy 235, 118–128. http://dx.doi.org/10.1016/j.solener.2022.02.013.
Bulfin, B., et al., 2013. Analytical model of $CeO_2$ oxidation and reduction. J. Phys. Chem. C 117 (46), 24129–24137. http://dx.doi.org/10.1021/jp406578z.
Chen, X., Xia, X.L., Liu, H., Li, Y., Liu, B., 2016. Heat transfer analysis of a volumetric solar receiver by coupling the solar radiation transport and internal heat transfer. Energy Convers. Manage. 114, 20–27. http://dx.doi.org/10.1016/j.enconman.2016.01.074.
Cooper, T., Steinfeld, A., 2011. Derivation of the angular dispersion error distribution of mirror surfaces for Monte Carlo ray-tracing applications. J. Sol. Energy Eng. 133 (4), http://dx.doi.org/10.1115/1.4004035.
Costa Oliveira, F.A., et al., 2020. High performance cork-templated ceria for solar thermochemical hydrogen productionviatwo-step water-splitting cycles. Sustain. Energy Fuels 4 (6), 3077–3089. http://dx.doi.org/10.1039/d0se00318b.
Cui, F., He, Y., Cheng, Z., Li, Y., 2013. Study on combined heat loss of a dish receiver with quartz glass cover. Appl. Energy 112, 690–696. http://dx.doi.org/10.1016/j.apenergy.2013.01.007.
Daabo, A.M., Al-Mola, Y.S., Al-Rawy, A.Y., Lattimore, T., 2019. State of the art single-objective optimization of small scale cylindrical cavity receiver. Sustain. Energy Technol. Assessments 35 (June), 278–290. http://dx.doi.org/10.1016/j.seta.2019.07.009.
Daabo, A.M., Mahmoud, S., Al-Dadah, R.K., 2016. The effect of receiver geometry on the optical performance of a small-scale solar cavity receiver for parabolic dish applications. Energy 114, 513–525. http://dx.doi.org/10.1016/j.energy.2016.08.025.
Daabo, A.M., Mahmoud, S., Al-Dadah, R.K., Ahmad, A., 2017. Numerical investigation of pitch value on thermal performance of solar receiver for solar powered Brayton cycle application. Energy 119, 523–539. http://dx.doi.org/10.1016/j.energy.2016.12.085.
Dähler, F. others, 2018. Optical design and experimental characterization of a solar concentrating dish system for fuel production via thermochemical redox cycles. Sol. Energy 170, 568–575. http://dx.doi.org/10.1016/j.solener.2018.05.085.
Dou, B. others, 2019. Hydrogen production from the thermochemical conversion of biomass: Issues and challenges. Sustain. Energy Fuels 3 (2), 314–342. http://dx.doi.org/10.1039/c8se00535d.
Ezbiri, M., et al., 2020. High redox performance of Y0.5Ba0.5CoO3-: $\delta$ for thermochemical oxygen production and separation. React. Chem. Eng. 5 (4), 685–695. http://dx.doi.org/10.1039/c9re00430k.
Fuqiang, W., Ziming, C., Jianyu, T., Yuan, Y., Yong, S., Linhua, L., 2017. Progress in concentrated solar power technology with parabolic trough collector system: A comprehensive review. Renew. Sustain. Energy Rev. 79, 1314–1328. http://dx.doi.org/10.1016/j.rser.2017.05.174.
Furler, P., Scheffe, J.R., Steinfeld, A., 2012. Syngas production by simultaneous splitting of $H_2O$ and $CO_2$ via ceria redox reactions in a high-temperature solar reactor. Energy Environ. Sci. 5 (3), 6098–6103. http://dx.doi.org/10.1039/c1ee02620h.
Furler, P., Steinfeld, A., 2015. Heat transfer and fluid flow analysis of a 4kW solar thermochemical reactor for ceria redox cycling. Chem. Eng. Sci. 137, 373–383. http://dx.doi.org/10.1016/j.ces.2015.05.056.
Garrido, J., Aichmayer, L., Abou-Taouk, A., Laumert, B., 2018. Experimental and numerical performance analyses of a dish-stirling cavity receiver: Geometry and operating temperature studies. Sol. Energy 170, 913–923. http://dx.doi.org/10.1016/j.solener.2018.06.031.
Gavagnin, G., Sánchez, D., Martínez, G.S., Rodríguez, J.M., Muñoz, A., 2017. Cost analysis of solar thermal power generators based on parabolic dish and micro gas turbine: Manufacturing, transportation and installation. Appl. Energy 194, 108–122. http://dx.doi.org/10.1016/j.apenergy.2017.02.052.
Hafez, A.Z., Soliman, A., El-Metwally, K.A., Ismail, I.M., 2017. Design analysis factors and specifications of solar dish technologies for different systems and applications. Renew. Sustain. Energy Rev. 67, 1019–1036. http://dx.doi.org/10.1016/j.rser.2016.09.077.
Harris, J.A., Lenz, T.G., 1985. Thermal performance of solar concentrator/cavity receiver systems. Sol. Energy 34 (2), 135–142. http://dx.doi.org/10.1016/0038-092X(85)90170-7.
Hasuike, H., Yoshizawa, Y., Suzuki, A., Tamaura, Y., 2006. Study on design of molten salt solar receivers for beam-down solar concentrator. Sol. Energy 80 (10), 1255–1262. http://dx.doi.org/10.1016/j.solener.2006.03.002.
Haussener, S., Hirsch, D., Perkins, C., Weimer, A., Lewandowski, A., Steinfeld, A., 2009. Modeling of a multitube high-temperature solar thermochemical reactor for hydrogen production. J. Sol. Energy Eng. Trans. ASME 131 (2), 0245031–0245035. http://dx.doi.org/10.1115/1.3097280.
Herron, J.A., Kim, J., Upadhye, A.A., Huber, G.W., Maravelias, C.T., 2015. A general framework for the assessment of solar fuel technologies. Energy Environ. Sci. 8 (1), 126–157. http://dx.doi.org/10.1039/c4ee01958j.
Hong, K., Yang, Y., Rashidi, S., Guan, Y., Xiong, Q., 2020. Numerical simulations of a Cu–water nanofluid-based parabolic-trough solar collector. J. Therm. Anal. Calorim. (0123456789), http://dx.doi.org/10.1007/s10973-020-09386-4.
Huang, W., Han, Z., 2012. Theoretical analysis of error transfer from the surface slope to the reflected ray and their application in the solar concentrated collector. Sol. Energy 86 (9), 2592–2599. http://dx.doi.org/10.1016/j.solener.2012.05.029.
Huang, W., Huang, F., Hu, P., Chen, Z., 2013. Prediction and optimization of the performance of parabolic solar dish concentrator with sphere receiver using analytical function. Renew. Energy 53, 18–26. http://dx.doi.org/10.1016/j.renene.2012.10.046.
Ishida, T., Gokon, N., Hatamachi, T., Kodama, T., 2014. Kinetics of thermal reduction step of thermochemical two-step water splitting using $CeO_2$ particles: Master-plot method for analyzing non-isothermal experiments. Energy Procedia 49, 1970–1979. http://dx.doi.org/10.1016/j.egypro.2014.03.209.
Jafrancesco, D. others, 2018. Optical simulation of a central receiver system: Comparison of different software tools. Renew. Sustain. Energy Rev. 94, 792–803. http://dx.doi.org/10.1016/j.rser.2018.06.028.
jia, T., Huang, J., Li, R., He, P., Dai, Y., 2018. Status and prospect of solar heat for industrial processes in China. Renew. Sustain. Energy Rev. 90, 475–489. http://dx.doi.org/10.1016/j.rser.2018.03.077.
Jilte, R.D., Nayak, J.K., Kedare, S.B., 2017. Experimental investigation on heat losses from differentially heated cylindrical cavity receiver used in paraboloid concentrator. J. Sol. Energy Eng. 139 (3), 031013. http://dx.doi.org/10.1115/1.4036255.
Johnston, G., 1995. On the analysis of surface error distributions on concentrated solar collectors. J. Sol. Energy Eng. 117 (4), 294–296. http://dx.doi.org/10.1115/1.2847843.
Johnston, G., 1998. Focal region measurements of the 20 $m^2$ tiled dish at the Australian National University. Sol. Energy 63 (2), 117–124. http://dx.doi.org/10.1016/S0038-092X(98)00041-3.
Keshtkar, M.M., Gandjalikhan Nassab, S.A., 2009. Theoretical analysis of porous radiant burners under 2-D radiation field using discrete ordinates method. J. Quant. Spectrosc. Radiat. Transfer 110 (17), 1894–1907. http://dx.doi.org/10.1016/j.jqsrt.2009.04.007.
Khan, M.S., Abid, M., Ali, H.M., Amber, K.P., Bashir, M.A., Javed, S., 2019. Comparative performance assessment of solar dish assisted s-$CO_2$ Brayton cycle using nanofluids. Appl. Therm. Eng. 148, 295–306. http://dx.doi.org/10.1016/j.applthermaleng.2018.11.021.
Kulahli, M.C., Akbulut Özen, S., Etemoglu, A.B., 2019. Numerical simulation of a parabolic trough collector containing a novel parabolic reflector with varying focal length. Appl. Therm. Eng. 161, 114210. http://dx.doi.org/10.1016/j.applthermaleng.2019.114210.
Li, H., Huang, W., Huang, F., Hu, P., Chen, Z., 2013. Optical analysis and optimization of parabolic dish solar concentrator with a cavity receiver. Sol. Energy 92, 288–297. http://dx.doi.org/10.1016/j.solener.2013.03.011.
Li, S., Xu, G., Luo, X., Quan, Y., Ge, Y., 2016. Optical performance of a solar dish concentrator/receiver system: Influence of geometrical and surface properties of cavity receiver. Energy 113, 95–107. http://dx.doi.org/10.1016/j.energy.2016.06.143.
Lilliestam, J., Labordena, M., Patt, A., Pfenninger, S., 2017. Empirically observed learning rates for concentrating solar power and their responses to regime change. Nat. Energy 2 (7), http://dx.doi.org/10.1038/nenergy.2017.94.

Loni, R., Kasaeian, A.B., Askari Asli-Ardeh, E., Ghobadian, B., 2016. Optimizing the efficiency of a solar receiver with tubular cylindrical cavity for a solar-powered organic Rankine cycle. Energy 112, 1259–1272. http://dx.doi.org/10.1016/j.energy.2016.06.109.

Lu, X., Luo, X., Tan, J.Z.Y., Maroto-Valer, M.M., 2021. Simulation of CO2 photoreduction in a twin reactor by multiphysics models. Chem. Eng. Res. Des. 171, 125–138. http://dx.doi.org/10.1016/j.cherd.2021.04.011.

Luo, Y., Du, X.Z., Yang, L.J., Yang, Y.P., 2014. Numerical simulation on the performance of a combination of external and cavity absorber for solar power plant. Energy Procedia 49, 428–437. http://dx.doi.org/10.1016/j.egypro.2014.03.046.

Ma, Z., Li, M.-J., He, Y.-L., Zhang, K.M., 2021. Effects of partly-filled encapsulated phase change material on the performance enhancement of solar thermochemical reactor. J. Clean. Prod. 279, 123169. http://dx.doi.org/10.1016/j.jclepro.2020.123169.

Mao, Q., Shuai, Y., Yuan, Y., 2014. Study on radiation flux of the receiver with a parabolic solar concentrator system. Energy Convers. Manag. 84, 1–6. http://dx.doi.org/10.1016/j.enconman.2014.03.083.

Marxer, D., Furler, P., Takacs, M., Steinfeld, A., 2017. Solar thermochemical splitting of $CO_2$ into separate streams of CO and $O_2$ with high selectivity, stability, conversion, and efficiency. Energy Environ. Sci. 10 (5), 1142–1149. http://dx.doi.org/10.1039/c6ee03776c.

März, T., Prahl, C., Ulmer, S., Wilbert, S., Weber, C., 2011. Validation of two optical measurement methods for the qualification of the shape accuracy of mirror panels for concentrating solar systems. J. Sol. Energy Eng. 133 (3), 1–8. http://dx.doi.org/10.1115/1.4004240.

Mehrpooya, M., Ghorbani, B., Hosseini, S.S., 2018. Thermodynamic and economic evaluation of a novel concentrated solar power system integrated with absorption refrigeration and desalination cycles. Energy Convers. Manage. 175, 337–356. http://dx.doi.org/10.1016/j.enconman.2018.08.109.

Montini, T., Melchionna, M., Monai, M., Fornasiero, P., 2016. Fundamentals and catalytic applications of $CeO_2$-based materials. Chem. Rev. 116 (10), 5987–6041. http://dx.doi.org/10.1021/acs.chemrev.5b00603.

Moradi, M., Mehrpooya, M., 2017. Optimal design and economic analysis of a hybrid solid oxide fuel cell and parabolic solar dish collector, combined cooling, heating and power (CCHP) system used for a large commercial tower. Energy 130, 530–543. http://dx.doi.org/10.1016/j.energy.2017.05.001.

Otake, T., Yugami, H., Yashiro, K., Nigara, Y., Kawada, T., Mizusaki, J., 2003. Nonstoichiometry of Ce1-XYXO 2-0.5X-$\delta$ (X=0.1, 0.2). Solid State Ion. 161 (1–2), 181–186. http://dx.doi.org/10.1016/S0167-2738(02)00873-1.

Pavlovic, S., Daabo, A.M., Bellos, E., Stefanovic, V., Mahmoud, S., Al-dadah, R.K., 2017. Experimental and numerical investigation on the optical and thermal performance of solar parabolic dish and corrugated spiral cavity receiver. J. Clean. Prod. 150, 75–92. http://dx.doi.org/10.1016/j.jclepro.2017.02.201.

Rasih, R.A., Sidik, N.A.C., Samion, S., 2019. Numerical investigation of direct absorption solar collector using nanofluids: A review. IOP Conf. Ser. Mater. Sci. Eng. 469 (1), http://dx.doi.org/10.1088/1757-899X/469/1/012059.

Reich, L., Bader, R., Simon, T., Lipiński, W., 2015. Thermal transport model of a packed-bed reactor for solar thermochemical $CO_2$ capture. Spec. Top. Rev. Porous Media 6 (2), 197–209. http://dx.doi.org/10.1615/.2015012344.

Roeb, M., Neises, M., Monnerie, N., Sattler, C., Pitz-Paal, R., 2011. Technologies and trends in solar power and fuels. Energy Environ. Sci. 4 (7), 2503–2511. http://dx.doi.org/10.1039/c1ee01128f.

Sandoval, O.R., Caetano, B.C., Borges, M.U., García, J.J., Valle, R.M., 2019. Modelling, simulation and thermal analysis of a solar dish/stirling system: A case study in Natal, Brazil. Energy Convers. Manage. 181, 189–201. http://dx.doi.org/10.1016/j.enconman.2018.12.005.

Scheffe, J.R., McDaniel, A.H., Allendorf, M.D., Weimer, A.W., 2013. Kinetics and mechanism of solar-thermochemical $H_2$ production by oxidation of a cobalt ferrite-zirconia composite. Energy Environ. Sci. 6 (3), 963–973. http://dx.doi.org/10.1039/c3ee23568h.

Shaner, M.R., Atwater, H.A., Lewis, N.S., McFarland, E.W., 2016. A comparative technoeconomic analysis of renewable hydrogen production using solar energy. Energy Environ. Sci. 9 (7), 2354–2371. http://dx.doi.org/10.1039/c5ee02573g.

Shuai, Y., Xia, X.-L., Tan, H.-P., 2008. Radiation performance of dish solar concentrator/cavity receiver systems. Sol. Energy 82 (1), 13–21. http://dx.doi.org/10.1016/j.solener.2007.06.005.

Tang, X.Y., Dou, P.Y., Dai, Z.Q., Yang, W.W., 2022. Structural design and analysis of a solar thermochemical reactor partially filled with phase change material based on shape optimization. Sol. Energy 236, 613–625. http://dx.doi.org/10.1016/j.solener.2022.03.041.

Tang, X.Y., Yang, W.W., Yang, Y., Jiao, Y.H., Zhang, T., 2021. A design method for optimizing the secondary reflector of a parabolic trough solar concentrator to achieve uniform heat flux distribution. Energy 229, 120749. http://dx.doi.org/10.1016/j.energy.2021.120749.

Tou, M., Jin, J., Hao, Y., Steinfeld, A., Michalsky, R., 2019. Solar-driven co-thermolysis of CO2 and H2O promoted by: In situ oxygen removal across a non-stoichiometric ceria membrane. React. Chem. Eng. 4 (8), 1431–1438. http://dx.doi.org/10.1039/c8re00218e.

Wendelin, T., 2003. Soltrace: A new optical modeling tool for concentrating solar optics. http://dx.doi.org/10.1115/ISEC2003-44090.

Wendelin, T., Dobos, A., Lewandowski, A., Wendelin, T., Dobos, A., 2013. SolTrace: A ray-tracing code for complex solar optical systems SolTrace: A ray-tracing code for complex solar optical systems. no. October.

Widyolar, B. others, 2019. Theoretical and experimental performance of a two-stage (50X) hybrid spectrum splitting solar collector tested to 600 °C. Appl. Energy 239, 514–525. http://dx.doi.org/10.1016/j.apenergy.2019.01.172.

Wu, Q., 2015. Handbook of Porous Media. CRC Press, http://dx.doi.org/10.1201/b18614.

Wu, Z., Caliot, C., Flamant, G., Wang, Z., 2011a. Coupled radiation and flow modeling in ceramic foam volumetric solar air receivers. Sol. Energy 85 (9), 2374–2385. http://dx.doi.org/10.1016/j.solener.2011.06.030.

Wu, Z., Caliot, C., Flamant, G., Wang, Z., 2011b. Coupled radiation and flow modeling in ceramic foam volumetric solar air receivers. Sol. Energy 85 (9), 2374–2385. http://dx.doi.org/10.1016/j.solener.2011.06.030.

Zeng, J., Yu, X., Xuan, Y., Li, Q., Liu, D., 2020. Direct solar thermochemical conversion of methanol into syngas: Via nanocatalysts at lower temperatures. Sustain. Energy Fuels 4 (4), 1693–1703. http://dx.doi.org/10.1039/c9se01227c.

Zhu, Q., Xuan, Y., 2017. Pore scale numerical simulation of heat transfer and flow in porous volumetric solar receivers. Appl. Therm. Eng. 120, 150–159. http://dx.doi.org/10.1016/j.applthermaleng.2017.03.141.

## Further reading

Jilte, R.D., Kedare, S.B., Nayak, J.K., 2013. Natural convection and radiation heat loss from open cavities of different shapes and sizes used with dish concentrator. Mech. Eng. Res. 3 (1), 25. http://dx.doi.org/10.5539/mer.v3n1p25.

Jilte, R.D., Kedare, S.B., Nayak, J.K., 2014. Investigation on convective heat losses from solar cavities under wind conditions. In: Energy Procedia, Vol. 57. http://dx.doi.org/10.1016/j.egypro.2014.10.197.